

Transition from homogeneous-like to shear-band deformation in nanolayered crystalline Cu/amorphous Cu–Zr micropillars: Intrinsic vs. extrinsic size effect

J.Y. Zhang, G. Liu^{*}, S.Y. Lei, J.J. Niu, J. Sun^{*}

State Key Laboratory for Mechanical Behavior of Materials, Xi'an Jiaotong University, Xi'an 710049, People's Republic of China

Received 13 April 2012; received in revised form 6 September 2012; accepted 10 September 2012

Available online 5 October 2012

Abstract

The microcompression method was used to investigate the compressive plastic flow behavior of nanolayered crystalline/amorphous (C/A) Cu/Cu–Zr micropillars within wide ranges of intrinsic layer thicknesses ($h \sim 5\text{--}150\text{ nm}$) and extrinsic sample sizes (350–1425 nm) with the goal of revealing the intrinsic size effect, extrinsic size effect and their interplay on the plastic deformation behavior. The nanolayered C/A micropillars exhibited deformation behaviors of strain-hardening followed by strain-softening that were dependent on the thickness of the layers. At $h \leq 10\text{ nm}$, the strain-softening is related to shear deformation that is caused by fractures in the amorphous layers. At $h > 10\text{ nm}$, however, the strain-softening is related to the reduction in dislocation density caused by dislocation absorption. Correspondingly, the deformation mode of the C/A micropillars transitioned from homogeneous-like to shear band type as h decreased to the critical value of $\sim 10\text{ nm}$, which is indicative of a significant intrinsic size effect. The extrinsic size effect on the plastic deformation also became remarkable when h was less than $\sim 10\text{ nm}$, and the interplay between the intrinsic and extrinsic size effects leads to an ultra-high strength of $\sim 4.8\text{ GPa}$ in the C/A micropillars, which is close to the ideal strength of Cu and considerably greater than the ideal strength of the amorphous phase. The underlying strengthening mechanism was discussed, and the transition in deformation mode was quantitatively described by considering the strength discrepancy between the two constituent crystalline and amorphous layers at different length scales.

© 2012 Acta Materialia Inc. Published by Elsevier Ltd. All rights reserved.

Keywords: Nanolayered film; Crystalline/amorphous micropillar; Plastic deformation; Size effect

1. Introduction

Metallic glasses (MGs) exhibit unique mechanical properties and deform via the shear transformation zones (STZs) in lieu of the well-defined plasticity carriers – dislocations in crystals [1–5]. In metallic crystals, it is well known that the motion of dislocations that are induced by a mechanical stress causes irreversible deformation through a shearing process. Strain hardening, which results from dislocation multiplication and interactions, leads to

stable and uniform elongation and tensile ductility [6,7]. However, the STZs in MGs cooperatively rearrange to accommodate the applied shear strain [3,8,9] and is often excited to a more energetic state (i.e., shear-softened) upon shear transformation [2,5]. After the plastic deformation begins, the STZs are readily linked in an autocatalytic manner to form a narrow shear band (SB), which causes highly catastrophic failure through rapid shear banding and consequently results in very low ductility at room temperature [8–10]. Therefore, the incorporation of MGs into engineering materials is often accompanied by complete brittleness or an apparent loss in tensile ductility, which significantly limits the structural applications for MGs. The formation of SBs in MGs must be fully understood and ultimately controlled for practical applications.

^{*} Corresponding authors. Tel.: +86 (0)2982 668695; fax: +86 (0)2982 663453.

E-mail addresses: lgammer@mail.xjtu.edu.cn (G. Liu), junsun@mail.xjtu.edu.cn (J. Sun).

Considerable efforts have been focused on eliciting and improving ductility in MGs. Reducing the sample dimensions to the nanoscale has been reported as a viable approach for suppressing catastrophic failure resulting from the instantaneous propagation of SBs [11–17]. Recently, an interesting report revealed that the glassy metals could exhibit a transition from the strong-yet-brittle to the stronger-and-ductile state, even at room temperature, if their physical dimensions were reduced to the sub-micrometer and specifically the nanometer scales [11,12,15]. The individual shear banding events have also been shown to be strongly size-dependent, i.e., the deformation is controlled by SB nucleation in larger sizes whereas it is controlled by SB propagation in smaller sizes [13,14]. The fracture strength of MGs can reach a significant level of the ideal strength $\sim E/30$ or $\sim \mu/10$ [4,12,15,18], where E and μ is the elastic and shear modulus, respectively.

In addition to confining the sample size [11,15], embedding deformable crystalline phases into the MG matrix to inhibit the propagation of SBs has been proposed as an alternative method for effectively enhancing the plastic deformability of MGs [19–21]. Similarly, suppressing the formation and propagation of SBs in the MGs is also possible by integrating amorphous and crystalline layers to form nanolayered materials [16,17,22–24]. Specifically, the integration of a crystalline/amorphous (C/A) nanolayered structure has been considered as a potential method for improving the deformability of the multilayers without sacrificing their strength. For example, Wang and coworkers [22] have reported that free-standing C/A Cu/Cu–Zr nanolaminates with respective thicknesses of 35/5 nm reliably exhibited high tensile strength (~ 1.2 GPa) and large tensile elongation ($\sim 14\%$). Furthermore the compression plastic strain of C/A X/Zr–Cu ($X = \text{Cu}, \text{Mo}, \text{Zr}$) layered pillars can reach greater than 55% when the thickness of the crystalline X layer is greater than ~ 200 nm [23]. The above experimental results [22–24] have clearly revealed that a multilayer scheme is likely to suppress the SBs and significantly improve the deformability of MGs by forming C/A multilayer architecture. However, the underlying mechanism for how the crystalline layers suppress the formation/propagation of the SBs in glassy layers is still unclear, especially in the nanoregime. In addition, whether the crystalline layers are still capable of suppressing the propagation of shear bands in the MGs layers when the crystalline layers are thinned to several nanometers, which is of scientific importance and technological relevance, remains to be determined. Consequently, the plastic deformation of nanostructured C/A multilayers warrants being thoroughly and systematically studied.

At the nanoscale, the interfaces between two constituent materials play an increasingly important role in determining the mechanical properties of multilayers [25–28]. The interfaces can act as [29]: (i) sources of dislocations, (ii) sinks of dislocations via absorption and annihilation, (iii) barriers to dislocations and (iv) storage sites for dislocations. Previous studies have often treated the role of interfaces in a

phenomenological way, which yields scaling laws such as the Hall–Petch (H–P) type-model based on dislocation pile-up [30], the confined layer slip (CLS) model that involves single dislocation loops that glide in isolated layers [31,32], and the interface barrier strength (IBS) model that assumes dislocation across the interface [33,34]. The above dislocation mechanisms have been employed to explain the intrinsic size effect on the deformation features/behaviors of crystalline/crystalline (C/C) multilayers [26,35,36]. However, the interfaces in nanostructured C/A multilayers (CAIs) that do not have a specific crystallographic orientation may exhibit unique inelastic shear (slip) transfer characteristics and relatively lower interface stress or energy due to the existence of the amorphous phase [22]. These interfaces are considerably different from the C/C interfaces (CCIs) and grain boundaries (GBs). Therefore, it is of significant interest to determine the effect of CAIs on the mechanical behaviors and deformation mechanisms of nanostructured C/A multilayers.

By using the microcompression method in this work, we illustrate the constraining effects of the crystalline layer on the amorphous layer at the nanoscale and address the correlations between the intrinsic size (layer thickness, h) and extrinsic size (pillar diameter, ϕ) on the mechanical response and deformation mode of nanolayered C/A Cu/Cu–Zr micropillars. The present results reveal that the competition between the intrinsic and extrinsic size effects results in a critical size of $h \sim 10$ nm, above which the deformation is predominantly dependent on the intrinsic size and insensitive to the pillar diameter, while below this critical size, the two size effects are comparable. The apparent deformation modes were observed to transition from homogeneous-like deformation to shear banding at this critical size. The influences of amorphous layers and CAIs on plastic deformation were discussed to rationalize the size-dependent strain-softening behavior, which was induced by failure of the amorphous layer when $h \leq 10$ nm and by the absorption of dislocations when $h > 10$ nm.

2. Experiment details

2.1. Sample preparation and microstructure characterization

C/A Cu/Cu–Zr multilayers were deposited on HF-etched Si (100) substrates by direct current (dc) magnetron sputtering at room temperature. Cu (99.995%) and Zr (99.99%) targets were used to produce alternating layers of nanocrystalline pure Cu and amorphous Cu₆₀Zr₄₀ (atomic fraction). The chamber was evacuated to a base pressure of $\sim 6.0 \times 10^{-8}$ Torr, and 1.0 – 2.5×10^{-3} Torr of Ar was maintained during the deposition process. The substrate was neither heated nor cooled during the deposition process. The constituent layers in the C/A multilayers have equal thicknesses of h ($h = h_a = h_c$), and a wide range of h ranging from 5 to 150 nm was designed to disclose the intrinsic size effect. During the deposition process, a 100-nm-thick Cu seed layer was first deposited on the Si

substrate, and the periodical amorphous/crystalline layers were subsequently deposited on the seed layer. The cap layer of the multilayer was always Cu. The Cu60Zr40 amorphous layer was synthesized by co-sputtering. The total thicknesses of the C/A Cu/Cu–Zr multilayers were $\sim 2 \mu\text{m}$ when $h < 100 \text{ nm}$ and $\sim 3.0 \mu\text{m}$ when $h \geq 100 \text{ nm}$. For comparison, $2 \mu\text{m}$ -thick single-layer pure Cu films and amorphous Cu60Zr40 films were also prepared on Si (100) substrates.

X-ray diffraction (XRD) experiments were performed on a Bruker D8 Discover powder X-ray diffractometer at room temperature. To identify the elemental composition and the interface integrity of the specimens, high resolution transmission electron microscopy (HRTEM) and energy dispersive X-ray (EDX) analyses were conducted on a JEOL JEM-2100F microscope, which is equipped with Fischione ultra-high resolution high-angle annular dark field detector (0.23 nm resolution in the STEM imaging mode) and an Oxford instruments EDX detector (spatial resolution of $\sim 1 \text{ nm}$) for chemical analysis.

2.2. Fabrication of nanolayered C/A micropillars

Nanolayered C/A Cu/Cu–Zr micropillars, with diameters ranging from 350 to 1425 nm, were fabricated from the as-deposited C/A multilayers using a Helios Nano Lab 600i dual-beam focused ion beam (FIB) system, which also allows scanning electron microscopy (SEM) imaging. The interface planes are strictly perpendicular to the cylinder axis. To minimize the potential damage from ion irradiation due to the Ga ion beam and to clean any newly deposited materials from the pillar surface, the final FIB fine milling step was performed under a lowered voltage (15 kV) and current (15 pA). A protective coating layer was not employed in the present work to avoid any other contribution to the mechanical response from the presence of foreign layers. The dimensions of the micropillars and the taper were measured from the SEM images. The aspect ratios (height to diameter, β) of the pillars varied between 2.0 and 6.0, whereas the taper angles (ψ) of the pillars were measured between 2° and 4° .

2.3. Flat punch compression test

The microcompression test was performed on a Hystron Ti 950 with a $10 \mu\text{m}$ side-flat quadrilateral cross-section diamond indenter. The alignment of the tip pillar was achieved with the help of an optical microscope. All of the micropillars were compressed under the displacement-controlled mode at a loading rate $\sim 0.4 \text{ nm s}^{-1}$ (corresponding to a constant strain rate of $2 \times 10^{-4} \text{ s}^{-1}$) up to 15–30% strain, which was followed by a holding segment of 5 s before unloading. Force–displacement data were continuously recorded, and the initial geometry of the pillar was measured from the SEM images. True stress–strain curves were calculated using a constant volume and

homogeneous deformation assumption model to characterize the deformation behaviors [37–39]. More details about the procedure used to calculate the true stress–strain curves can be found in Refs. [37–39]. After accounting for the substrate effect and correcting for taper, the true strain (ε_T) and true stress (σ_T) are simply expressed as:

$$\begin{aligned} \varepsilon_T &= \frac{1}{E_m} \frac{PL_p}{A_0 L_0} + \ln \left(\frac{L_0}{L_p} \right) \\ &= \frac{1 + \frac{L_0}{r_0} \tan \psi}{E_{\text{measured}}} \frac{PL_p}{A_0 L_0} + \ln \left(\frac{L_0}{L_p} \right) \end{aligned} \quad (1)$$

and

$$\begin{aligned} \sigma_T &= \frac{P}{A_p} = \frac{PL_p}{A_0 L_0} \\ &= \frac{P}{A_0 L_0} \left\{ L_0 - \left[u_{\text{tot}} - \frac{PL_{\text{Si}}}{E_{\text{Si}} A_{\text{Si}}} - \frac{\sqrt{\pi} P (1 - \nu_m^2)}{2 E_{\text{Si}} \sqrt{A_{\text{Si}}}} \right] \right\} \end{aligned} \quad (2)$$

where A_0 is the cross-sectional area at half of the initial height (L_0) of the pillar, r_0 is the radius at the top of the pillar, L_p and A_p are the final height and average cross-sectional areas, respectively, P is the applied load, E_m is the true modulus of the C/A pillars without tapers and E_{measured} is the measured modulus of the tapered C/A pillars, u_{tot} is the total displacement, ν_m is Poisson's ratio of the C/A multilayers (~ 0.33) and A_{Si} , L_{Si} and E_{Si} are the average cross-sectional area, the total length and the modulus of the Si substrate, respectively. Note that the influence of taper (ψ) has been considered in the above equations. Furthermore, note that the deformation within 10% strain could be simply regarded as homogeneous, and the work-hardening parameter derived from the true stress–strain curves could be approximately used to investigate both the intrinsic and extrinsic size effects on the deformation behaviors of nanolayered C/A pillars.

2.4. Correction of thermal drift

Because of the amount of time (~ 750 – 1500 s) required to conduct the vast majority of compression experiments, considerable efforts have been devoted to correcting for thermal drift to improve the reliability and accuracy of the present nanoscale deformation measurements. The microcompression test system provides the option of an allowable drift rate (ADR) to set the thermal stability criterion for initiating the testing. Although the flat punch indenter is in contact with the top surface under a small constant force, the time rate of change in the displacement must be less than the chosen value of the ADR. In the present work, the ADR was set at 0.005 nm s^{-1} , which is 20 times smaller than the typical value (0.1 nm s^{-1}) used in the testing of films/micropillars such that the effect of thermal drift could be minimized and neglected. To achieve even better precision of the mechanical response of the specimens, a minimum of five effective tested data were used for subsequent analyses.

3. Results

3.1. Microstructure of nanolayered C/A multilayers

The XRD patterns of the as-deposited C/A Cu/Cu–Zr multilayers in Fig. 1 reveal that the multilayers exhibit Cu (111) and Cu (200) peaks, and the Cu (111) peak broadens with decreasing h . However, the Cu (200) peaks remain the same, which can be attributed to the use of the Cu seed layer. The peak intensity of glassy Cu₆₀Zr₄₀ is quite low in all of the C/A multilayers, which is in good agreement with the observed weak amorphous humps in the monolithic amorphous films in the diffraction angle range (2θ) of 35–45°.

The microstructures of the cross-sections of the C/A multilayers were examined in detail using TEM, as shown in Fig. 2. The bright field TEM micrograph of the $h = 50$ nm C/A multilayers reveals drastic contrast differences between nanocrystalline Cu and the amorphous Cu–Zr layers, as shown in Fig. 2a, from which one can clearly observe the modulated layered structure. The selected area diffraction pattern (SADP) that is shown in the inset of Fig. 2a also exhibited a diffuse amorphous ring. A similar amorphous structure was observed in the $h = 5$ nm C/A multilayers through HRTEM micrographs and the fast Fourier transform (FFT) of region II (RII) in Fig. 2b. In all of the C/A Cu/Cu–Zr multilayers, the CAIs are quite distinguishable.

3.2. Mechanical response of nanolayered C/A micropillars

Representative true stress–strain curves for the $h = 10$ and 50 nm Cu/Cu–Zr pillars are presented in Fig. 3a and b, respectively, with variation in pillar size ϕ . The comparison of the figures clearly reveals that the smaller h or ϕ pillars exhibit a higher flow stress. Note that all of the C/A pillars display three regimes in the true stress–strain curves, as marked in Fig. 3a and b. Regime I is the linear elastic regime and ends at the yield point (σ_0), which occurs at

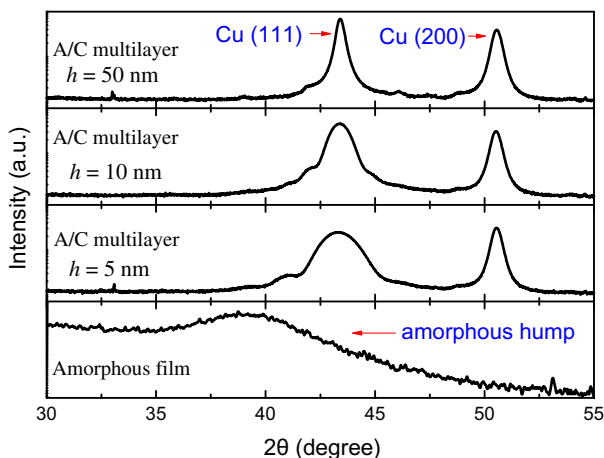


Fig. 1. XRD patterns for the C/A Cu/Cu–Zr multilayers and monolithic amorphous films.

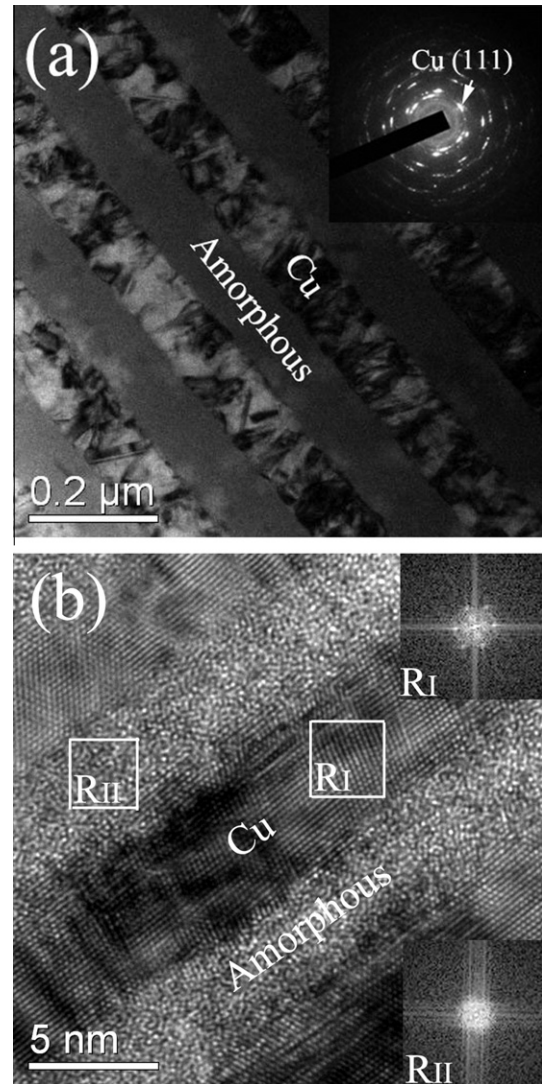


Fig. 2. TEM images of (a) $h = 100$ nm and (b) $h = 5$ nm for the C/A multilayers. Inset in (a) is the SADP that reveals strong Cu (111) texture in Cu layer. Insets in (b) are the fast Fourier transform (FFT) for the Cu layer (RI) and amorphous layer (RII), respectively.

the strain (ε) of ~ 0.03 . Regime II exhibits a strain-hardening behavior, which ends at $\varepsilon \sim 0.1$. By assuming that the strain-hardening equation is still valid at the nanoscale [40–42], the strain-hardening behavior in regime II can be described by Ludwik's equation, as follows [26]:

$$\sigma = K_1 + K_2 \varepsilon_p^n \quad (3)$$

where K_1 is the initial yield stress, K_2 is the strengthening coefficient (i.e., the increase in strength due to strain-hardening at plastic strain, $\varepsilon_p = 1$), and n is the strain-hardening exponent. By taking $K_1 = \sigma_0$, Eq. (3) can be used to fit the true stress–strain curves in regime II with good agreement, as, respectively shown in Fig. 2a and b. The strain-hardening rate, Θ , in this regime is then estimated by using the following equation [26,41,42]:

$$\Theta = \frac{d\sigma}{d\varepsilon} = \frac{n(\sigma_{2\%} - \sigma_{0.2\%})}{(\varepsilon_{2\%} - \varepsilon_{0.2\%})} \quad (4)$$

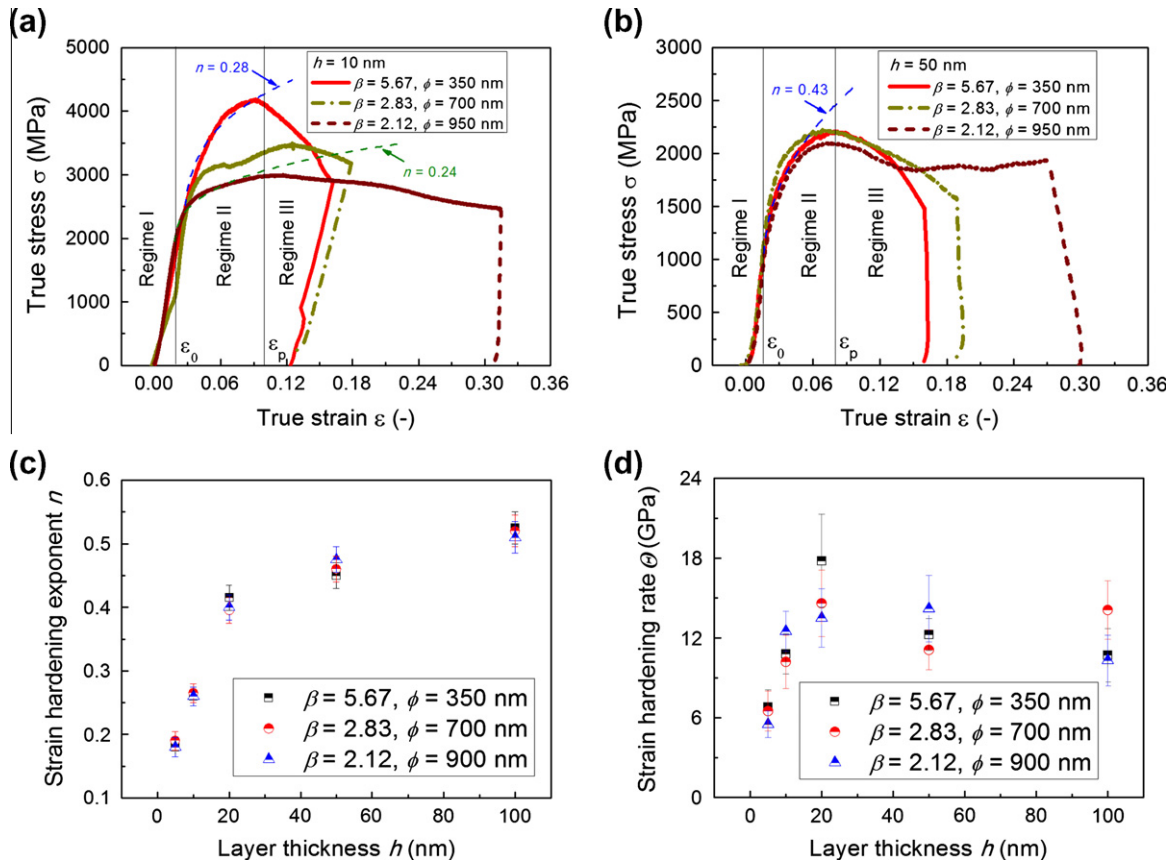


Fig. 3. True stress–strain plot for (a) $h = 10$ nm and (b) $h = 50$ nm C/A micropillars with various ϕ . Load is applied perpendicular to the layer interface. The strain-hardening regime (regime II) is fitted using Eq. (3). (c) and (d) are the strain-hardening exponent (n) and the strain-hardening rate (θ), respectively, as a function of h for the C/A micropillars with three different ϕ .

where $\sigma_{0.2\%}$ and $\sigma_{2\%}$ are the strengths at plastic strains of $\epsilon_p = 0.2\%$ ($\epsilon_{0.2\%}$) and $\epsilon_p = 2\%$ ($\epsilon_{2\%}$), respectively. The strain-hardening exponent, n , and the strain-hardening rate, θ , were quantitatively evaluated, and their dependence on ϕ as a function of h is shown in Fig. 3c and d, respectively. n is remarkably dependent on h but insensitive to the pillar size, ϕ . The value of n monotonically decreases from ~ 0.50 to ~ 0.17 as h decreases from 100 to 5 nm (Fig. 3c). Similarly, the strain-hardening rate, θ , is also intrinsically size-controlled and slightly affected by ϕ . However, the variation of θ with h is non-monotonic and θ reaches a maximum of ~ 16 GPa at $h \sim 20$ nm, as shown in Fig. 3d. The Cu/Cu–Zr pillars display θ values that are considerably greater than that of the bulk Cu (~ 2.5 GPa [6]). In regime III, strain-softening generally occurred with strains greater than ~ 0.1 . The strain-softening is also more pronounced when h or ϕ are smaller. Notably, it is intriguing to observe that no strain burst was observed in any of the compressive curves.

3.3. Mechanical response of single-phase amorphous micropillars

Shear banding appears to be the dominant plasticity mode in the single-phase amorphous samples, even in the

micron- and submicron-sized micropillars, as shown in Fig. 4. Fig. 4a presents typical true stress–strain curves of three single-phase amorphous Cu₆₀Zr₄₀ pillars with $\phi = 600, 800$ and 1200 nm. Fig. 4b–d and its insets are the corresponding SEM micrographs of the amorphous pillars before and after the test. A shear band is observed to initiate at the side surface and run across the entire pillar (hereafter referred to as a mature or major shear band). The formation of such shear bands inevitably leads to a strain burst or stress drop in the true stress–strain curves (Fig. 4a), which is a typical deformation behavior of amorphous materials that are compressed at room temperature. Therefore, these true stress–strain curves are characterized by segments of elastic loadings, which cause even higher stresses and activate shear banding events that are followed by rapid and discrete bursts. In sharp contrast to the plastic flow of crystalline Cu pillars (not shown here) and C/A pillars where more severe deformation leads to defect accumulation and induces strain-hardening, the stored elastic energy in the amorphous pillars is released through the discrete bursts in the small-scale deformation. The occurrence of bursts weakens the subsequent elastic energy storage capability. In addition, comparison among the true stress–strain curves reveals that, with decreasing pillar diameter, the abrupt shear processes become increasingly

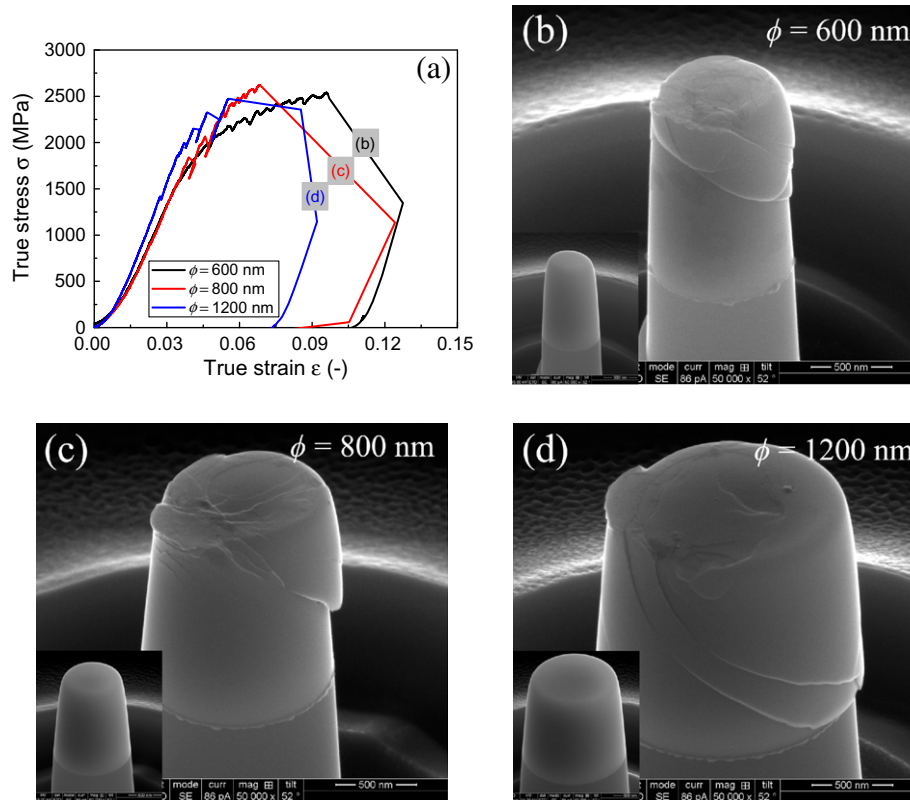


Fig. 4. (a) True stress–strain plot for the amorphous pillars with $\phi = 600$, 800 and 1200 nm and the corresponding SEM images of the tested pillars with $\phi = 600$ nm (b), $\phi = 800$ nm (c) and $\phi = 1200$ nm (d). Inset is the corresponding SEM images of the as-milled pillar.

mild. The shear displacement in the smaller pillars proceeds more smoothly; therefore, the stress decreases more steadily, which is in agreement with the observations of diffuse SBs, see Fig. 4b–d.

3.4. Strength of nanolayered C/A micropillars and the constituents

The plastic behavior of the C/A micropillars depends not only on their intrinsic size but also on their extrinsic size. Fig. 5a reveals a significant increase in the maximum strength, σ_{\max} (at $\epsilon_p \approx 8\%$), when the layer thickness, h , is reduced, which is similar to the behavior observed in the C/C Cu/Zr pillars [26]. The diameter ϕ dependence of σ_{\max} is quite weak when $h > 10$ nm, whereas it becomes considerably stronger when $h < 10$ nm. This result suggests that the extrinsic size effect is remarkable only at small values of h . In Fig. 5a, some experimental results from other studies are also presented for comparison, including the ϕ -dependent strength of amorphous pillars [14,15] and the h_a -dependent fracture strength of the C/A Cu/Cu50Zr50 nanolaminates [17]. The single-phase amorphous pillars appear to have a ϕ -independent strength of $\sim 1850 \pm 350$ MPa within the wide ϕ range from 100 to 1000 nm, which is considerably greater than the reported maximum strength of pure Cu of ~ 1250 MPa (Fig. 5b). The present C/A pillars, however, can reach an ultrahigh strength of ~ 4800 MPa under the

coupling effect by both intrinsic and extrinsic size constraining ($h = 5$ nm and $\phi = 350$ nm), which is ~ 2.4 times the strength of the pure amorphous pillars. Note that the ideal strength of Cu60Zr40 glass is $\sim E/30 = 3$ GPa [15,17,18,43] (see the green dash-dot line in Fig. 5a), which is still far less than the maximum strength achieved in the nanolayered C/A pillars.

Fig. 5b presents an additional comparison between the present C/A multilayer with various Cu structures reported in the available literature, including single crystal Cu pillars [44], Cu nanowhiskers [45], polycrystalline Cu films [46,47] and nanotwinned Cu [48]. This figure clearly reveals that (i) the strength of polycrystalline Cu gradually increases when the characteristic dimension decreases (diameter, ϕ , or the film/twin thickness, h) to the nanometer scale and then appears to decrease as the characteristic dimension decreases to less than ~ 20 nm, and (ii) only the pristine and defect-free Cu nanowhiskers that were presented in previous reports have a strength that is close to the theoretical upper limit. In contrast, the present C/A Cu/Cu–Zr pillars have a strength that is progressively increased with reducing h , even down to 5 nm, when the pillar size is less than 950 nm. At $\phi = 350$ nm and $h = 5$ nm, the strength of the C/A pillar reaches 4800 MPa, which is close to the theoretical upper limit of Cu. This result indicates that the nanolayered structure may offer significant benefits for extending the strength limit of Cu, which provides an

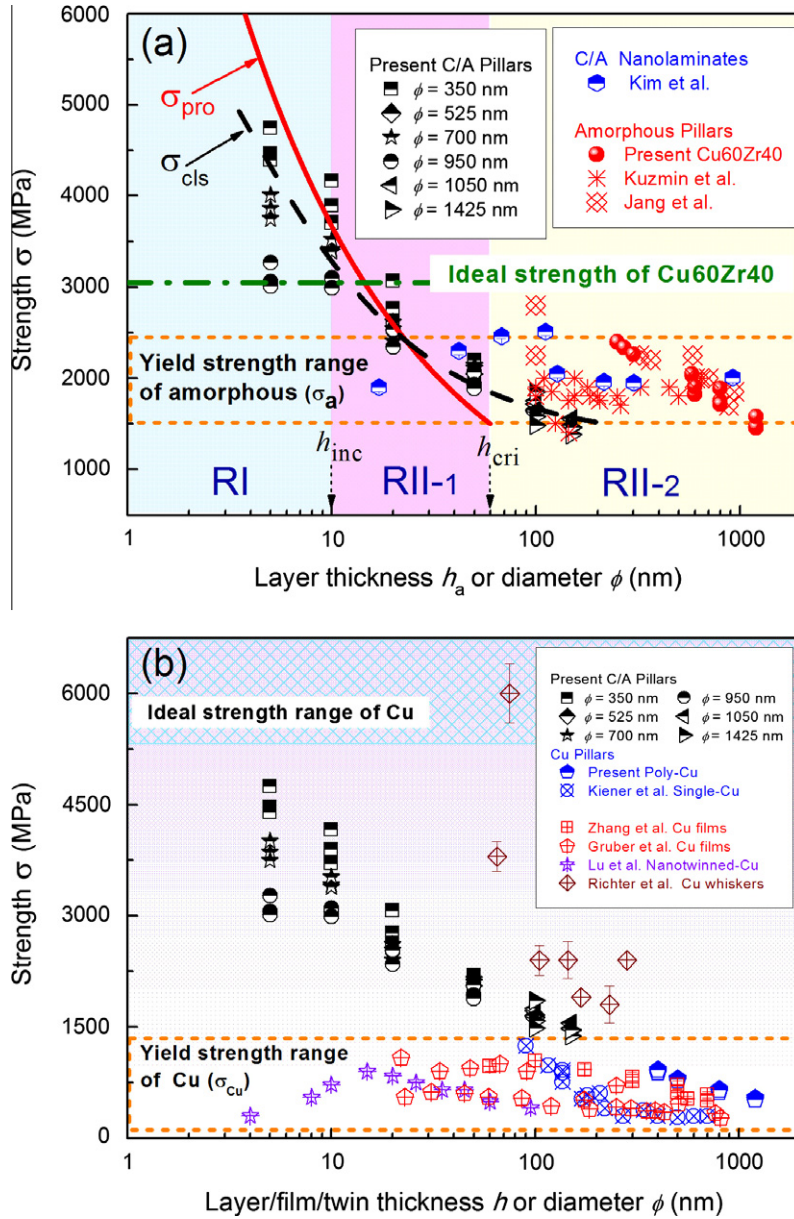


Fig. 5. (a) Dependence of the maximum strength of C/A pillars on pillar diameters as a function of amorphous layer thickness (h_a). For comparison, others' reports on the h_a -dependent fracture strength of C/A Cu/Cu–Zr nanolaminates (Kim et al. [17]) and diameter ϕ -dependent yield strength amorphous pillars (Kuzmin et al. [14] and Jang et al. [15]) are also included in this figure. The confined layer slip stress (σ_{cls}) for dislocation glide in the Cu layer and the required stress (σ_{pro}) for SB propagation in the amorphous layer as well the ideal strength of amorphous Cu60Zr40 are also plotted. (b) The maximum strength of C/A pillars as a function of layer thickness and that of polycrystalline Cu pillars as a function of diameter. Also presented in this figure are the reported strengths of single crystal Cu pillars [44] and Cu whiskers [45] as a function of diameter, Cu thin films [46,47] as a function of film thickness and nanotwinned Cu [48] as a function of twin thickness. Regime I (RI) and regime II (RII) represent shear band deformation and homogeneous-like deformation, respectively.

effective route for developing advanced ultrahigh-strength materials.

3.5. Deformation behavior of the nanolayered C/A micropillars

Fig. 6a–h and their insets present SEM images of C/A micropillars with different h and/or ϕ before and after compression. After compression, the $h = 10$ and 5 nm pillars

display shear deformation across the compression plane without significant extrusion, which is indicative of a shearing regime at $h \leq 10$ nm. From the SEM/FIB micrographs, note that as ϕ decreases from 950 to 350 nm (or β increases from 2.12 to 5.67), there is an apparent transition in the shearing mode from highly inhomogeneous shear (pillar sheared within a mature/major SB [13]) to relatively homogeneous shear (pillar sheared at the rounded top part [13]) at this shearing regime. In other words, the well-developed

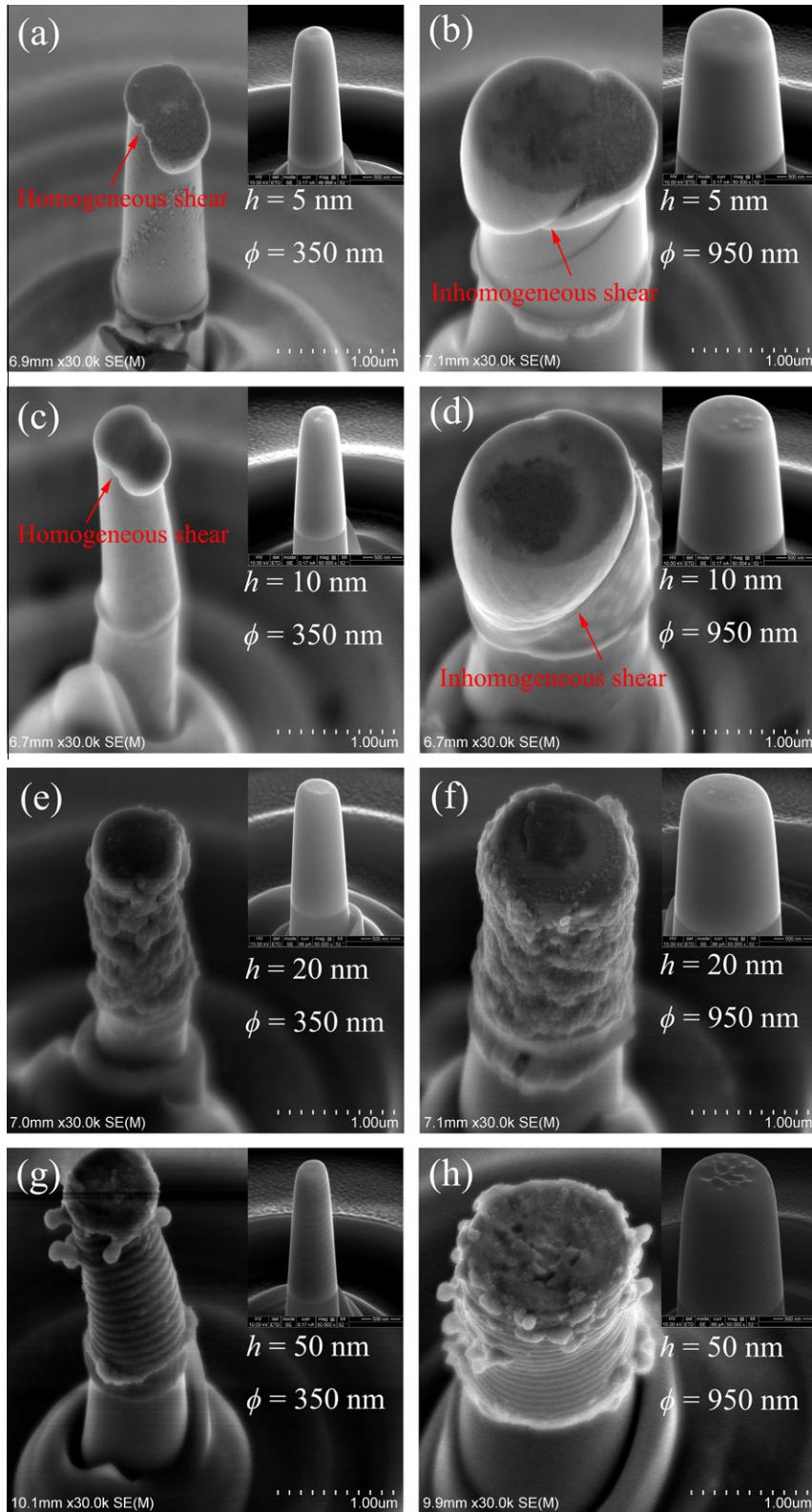


Fig. 6. Typical SEM images of nanolayered C/A micropillars with four different h after the uniaxial compression tests. (a) $\phi = 350$ nm and (b) $\phi = 950$ nm micropillars with $h = 5$ nm show barreling of the micropillar and extrusion of individual Cu layers; (c) $\phi = 350$ nm and (d) $\phi = 950$ nm micropillars with $h = 10$ nm show squeezing and shearing of the pillar; and (e) $\phi = 350$ nm and (f) $\phi = 950$ nm micropillar with $h = 20$ nm, and (g) $\phi = 350$ nm and (h) $\phi = 950$ nm micropillars with $h = 50$ nm show shear deformation. Inset is the corresponding SEM images of the as-milled pillar.

major SB with a sharp leading front at large ϕ (or small β) is gradually changed to shear deformation with rounded leading fronts at the upper part of the pillars. It is suggested that the deformation mode of the C/A micropillars can be simultaneously influenced by h and ϕ at small $h \leq 10$ nm. Similar phenomena have also been observed in C/C Cu/Zr [26,41], Al/Pd [49] and Cu-based amorphous [13] pillars. These results indicate that the shear deformation in the larger pillars is controlled by nucleation of the SBs, but it becomes controlled by propagation in the smaller pillars [13,26].

In contrast, all of the $h > 10$ nm pillars exhibit plastic barreling and extrusion of soft Cu layers after compression, which have been demonstrated by careful microstructural examinations. Fig. 7a is a SEM/FIB image of the $h = 50$ nm C/A pillar that was compressed to 20% strain. Energy analysis at a point of the most upper extrusion layer reveals that the area is predominantly composed of elemental Cu, as shown in Fig. 7b. Additional SEM/FIB cross-sectional images also demonstrate that the thinning of the soft Cu layers dominates the plastic deformation

process, whereas plastically deforming the hard, amorphous Cu–Zr phase is difficult (see Fig. 7c and d). Fig. 7c and d also reveals that the extrusion of the Cu layers is favorably homogeneous, not only within a single layer but also among different layers from the top to the bottom. The taper morphology thus has a minor effect on the deformation behaviors of the nanolayered C/A pillars, which may be due to the very small taper angle. Another important conclusion that one can draw is that the homogeneous-like deformation in the $h > 10$ nm pillars is predominantly intrinsic size h -related and insensitive to the extrinsic size ϕ , which is in agreement with Fig. 6e–h.

4. Discussion

4.1. Size effect on the deformation behaviors of C/A micropillars

4.1.1. Strain hardening behaviors

The strain-hardening exponent (n) is an important parameter that signifies the strain-hardening or work-hardening

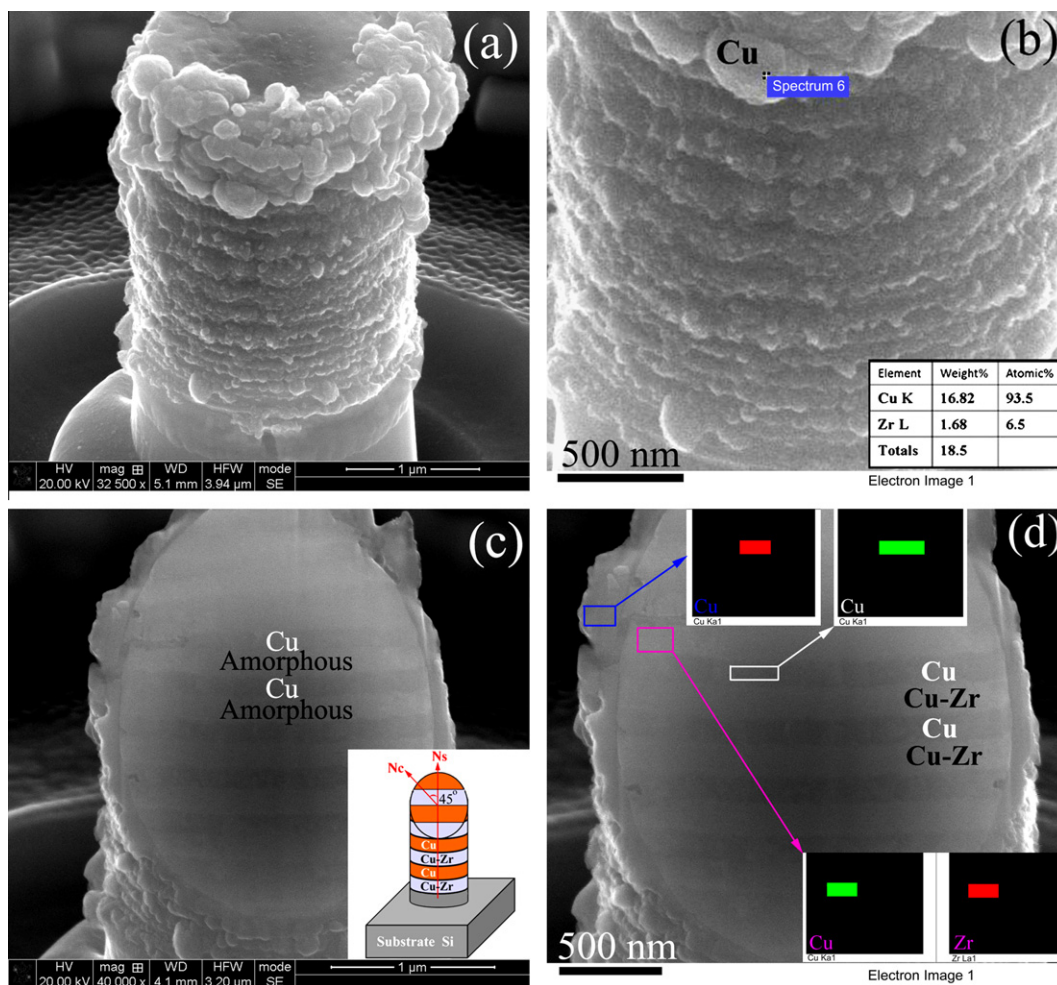


Fig. 7. (a) SEM micrograph showing the Cu/Cu–Zr pillar compressed to $\sim 20\%$ strain, (b) the energy point analysis proving the extruded materials is Cu, (c) the cross-sectional image of the FIB-ed deformed pillar (with 45° direction to the normal of the pillar top surface, see the inset), showing the layered structure and uniformly thinned Cu layers, and (d) the energy mapping analysis of three different regions (R1, R2, R3), proving that uniform thinning and extrusion of Cu layer. R1 is the extruded Cu, R2 is the amorphous Cu–Zr layer and R3 is the Cu layer.

characteristic of a material [40,50]. In the present nanolayered C/A pillars, n is controlled by the intrinsic rather than the extrinsic size. As shown in Fig. 3c, n monotonically decreased with decreasing h . This trend is analogous to that observed in polycrystalline Cu [48], nanolayered Al/TiN [42] and Cu/Zr [26,41] pillars. Therefore, the uniform deformability of the multilayers is suggested to monotonically decrease with reducing h [40], which is consistent with the SEM observations presented in Fig. 6. In larger sized metals (e.g., bulk metals), a high value of n was attributed to the multiplication and interactions of dislocations and the high dislocation storage capacity [6,51]. In contrast, in smaller sized metals (e.g., nanocrystalline metals), a decrease in the n value has been generally observed. This behavior can be interpreted in terms of the weak dislocation interactions and diminished dislocation accumulation because the dislocation emitted from the boundaries can easily move across the grain interior and be absorbed by the opposite boundaries [52,53]. In Fig. 4c, n is observed to be independent of the extrinsic size ϕ , which indicates that the dislocation interaction or dislocation density changes slightly as ϕ is varied at a given h . Specifically, the Cu/Cu–Zr pillars exhibit relatively higher n values at $h > 20$ nm, which are almost equal to that of bulk Cu (~ 0.4 – 0.5) [54,55]. However, below the critical transition size of $h \sim 10$ – 20 nm, the value of n is extremely low and even approaches that of the nanocrystalline metals (~ 0.1 – 0.2) [48]. This result is most likely arises because the dislocations are nucleated from different sources (e.g., from volume sources or from surface/interface sources [56]) within the two regimes above and below the transition size of $h \sim 10$ – 20 .

The strain-hardening rate (Θ) is another important parameter for characterizing the strain-hardening behavior of metals, which is closely linked to the stored dislocation density (ρ) [6,7]. It is quite interesting to observe that the intrinsic size-dependent Θ initially increases with decreasing h and reaches a maximum at the critical size of $h \sim 20$ nm, below which Θ decreases with further reducing h (Fig. 3d). A similar inverse h effect on Θ has also been observed in previous reports, including in pure Cu films [47] (with thickness ranges from 20 to 800 nm) and Cu/Zr multilayers [26,41] (with h from 5 to 100 nm). In the regime $h \geq 20$ nm, the increased dislocation–interface interactions cause the increase in Θ with reducing h , below which the dislocation cross-slip lowers Θ [26]. The underlying physical mechanism for this behavior is the h -dependent dislocation storage capacity, which has been quantitatively and simply explained in terms of a reduced dislocation storage rate [41].

4.1.2. Strain softening behaviors

Strain-softening behavior is generally observed in the stress–strain curves of the C/A micropillars, i.e., regime III. Although the shear-banding mechanism can be used to well explain the softening behavior of smaller h C/A

micropillars [26] (and the amorphous pillar [1–5,9,10]), it does not work at larger sizes of $h > 10$ nm because the shear deformation is now suppressed. In this case, the softening phenomenon is most likely caused by the reduction in dislocation density, which occurs through dislocation annihilation at large strains or the so-called work-softening [57,58]. The rationale behind this argument is that the amorphous layers can significantly impact the dislocation structures that formed in the nanocrystalline layers, as proposed by Wang et al. [22]. The authors have experimentally observed [22] that the C/A Cu/Cu–Zr nanolaminates possessed an exceptional tensile elongation of $\sim 14\%$. It was then postulated that the interplay between nanocrystalline layers and the nanoscale metallic glass may be the primary reason for the considerably enhancement in ductility, which was subsequently confirmed by molecular dynamics simulations. The simulation results [22] clearly revealed that the large defect cluster that evolved out of the amorphous phase was stopped by the nanocrystalline layers before it reached maturity. At the same time, the dislocation structures and geometric incompatibilities in the nanocrystalline layers were disturbed and dissolved by the amorphous layers. It was revealed that the CAIs can act as natural sinks for dislocations and absorb the dislocation content in the nanocrystalline Cu formed during plastic work. This process will cause a significant decrease in the amount of dislocations or the dislocation density and cause the work-softening, as observed in the present nanolayered C/A pillars. Note that near-perfect elastoplasticity was observed in the experiments reported by Wang et al. [22], whereas work-softening is observed in the present experiments. This discrepancy can be related to the difference in the relative content between the two constituent phases. In the work by Wang et al. [22], the nanocrystalline Cu layers have a thickness that is approximately seven times greater than that of the amorphous layers. The near-perfect elastoplasticity observed by Wang et al. hints that the newly activated dislocations in the nanocrystalline layers should be in equilibrium with those accumulated in the CAIs or absorbed by the amorphous layers. When the relative thickness of the amorphous (or crystalline) layers is increased (or decreased), the dislocation absorption/accumulation capability sharply overwhelms the dislocation activation capability, which results in reduced dislocations and work-softening. This behavior is the case in the present work, where the modulation ratio between the Cu layers to Cu–Zr layers is only 1, which is considerably less than the value of ~ 7 that was reported by Wang et al. [22]. Therefore, the fraction- or h -related dislocation-absorbing ability of the amorphous layer is also a reasonable explanation for another important finding in the present work: the work-softening is more severe for thinner values of h . Because more CAIs are present in the smaller h multilayers, the absorbing capability of the dislocations will be significantly enhanced and the dislocations should be further reduced in the nanocrystalline layers.

4.2. Strength of the C/A micropillars

Plastic deformation in nanolayered materials is distinct from that in single-phase films because of the presence of abundant hetero-phase interfaces. The high strength of C/A multilayers can be attributed to the hetero-phase interfaces constraining the dislocation activities. In the metallic multilayers composed of soft/ductile layers and hard/brittle layers, plastic flow is controlled by the soft/ductile phase [25,26,33,42]. In the present nanostructured C/A multilayers, the stress required to drive a single dislocation glide in an isolated ductile Cu layer (defined the confined layer slip or the CLS model) can be expressed as [25,26,33,42]:

$$\sigma_{\text{cls}} = M \frac{\mu^* b}{8\pi h'} \left(\frac{4-\nu}{1-\nu} \right) \ln \frac{\alpha h'}{b} + \frac{\mu^* b}{L(1-\nu)} - \frac{f}{h} \quad (5)$$

where $M \sim 3.06$ is the Taylor factor; $h' = h_{\text{Cu}}/\sin \phi$ is the thickness of the layer parallel to the glide plane, $\phi \sim 70.5^\circ$ is the angle between the slip plane and the interface, $b \sim 0.2556$ nm is the absolute length of the Burgers vector, $\nu \sim 0.343$ is the Poisson ratio of Cu, $\mu^* = (\mu_A \cdot \mu_{\text{Cu}})/(V_A \cdot \mu_{\text{Cu}} + V_{\text{Cu}} \cdot \mu_A)$ is the effective shear modulus of the C/A multilayer and can be estimated by the shear modulus (μ_{Cu}) and volume fraction (V_{Cu}) of the Cu layer and those of the amorphous layer; the geometrical factor $\alpha \sim 0-1$ represents the core cut-off parameter and contains the contribution of the extrinsic size constraint effect on the strength; L is the mean spacing of glide loops in a parallel array; and $f \sim 0.5-1.1$ J m⁻² is the characteristic interface stress of the C/A multilayer [59]. Taking $\alpha = 0.55$, $L = 12.5$ nm, $\mu^* = 40.6$ GPa and $f = 1.0$ J m⁻² in Eq. (5), the CLS model yields results that are in broad agreement with experimental data as h decreases from ~ 150 nm to ~ 10 nm (see dashed black line in Fig. 5a). At h values larger than ~ 150 nm, the CLS model considerably overestimates the strength of Cu. The well-known Hall–Petch model (dislocation pile-up strengthening mechanism) is more applicable in this regime [25,26,33,42]. As h less than ~ 10 nm, the influence of ϕ on the strength is quite marked, as mentioned in the above section. This result hints that considering the ϕ dependence is beyond the CLS prediction and that the quantitative description of strength should be expanded to include the sample size effect.

The marked ϕ dependence on strength observed at $h \leq 10$ nm can be explained as follows. When the intrinsic size decreases to this scale, the probability that the smaller volumes contain any dislocations is considerably reduced, and eventually, the dislocation is produced predominantly from surface/interface sources. In other words, the influence of the surface on the dislocation structure/activities is comparable with that of interfaces, which is likely the origin of the interplay between the extrinsic and intrinsic size effects. In contrast, the dislocation activities are predominantly controlled by the volume elements (i.e., individual grains) at $h > 10$ nm, which exclusively displays the intrinsic size effect.

4.3. Size effect on deformation mechanisms of C/A micropillars

4.3.1. Homogeneous-like deformation vs shear-band deformation

Donohue et al. [60] have reported that, by confining nanoscale glassy layers with a ductile nanocrystalline material as in multilayer structure, the formation of SBs can be suppressed. However, two requisites should be satisfied, as follows: (i) the crystalline layers are sufficiently stiff to produce a substantial elastic restoring force to counteract the nucleation of surface steps required for extensive shear events in the MG, and (ii) the crystalline layers are sufficiently thin such that the dislocation pileups can be suppressed and the crystalline layers will deform together with the high-strength amorphous layers.

When $h > 10$ nm, microstructural analyses reveal that the soft Cu layers between the amorphous Cu–Zr layers are preferentially thinned and squeezed out due to the strength disparity between the two constituent phases. This process is responsible for the plastic barreling observed in the present C/A pillars, which is similar to the behavior observed in previous C/A Cu/Cu50Zr50 pillars [23] and C/C Al/Pd [49] and Cu/Zr [26,41] pillars deformed under compression. The uniform thinning and extrusion of the Cu layer can be attributed to the symmetric slip activity of a single dislocation in the isolated crystalline layer and the CAIs with low shear strength that are susceptible to sliding [22,26,60]. Wang et al. [22] have mentioned that, as the deformation begins, a few STZs could be activated in an uncorrelated fashion inside the amorphous layers. When a dislocation nucleated from the CAI contacts the opposite CAI, more STZs are activated in a correlated fashion near the intersection line between the dislocation slip plane and the CAI [22,61]. Subsequently, the activated STZs trigger other STZs nearby, and the entire inelastically deformed zone gradually “diffuses” into the deeper amorphous region [22]. It is generally known that the spatial distribution of the STZ under applied stress determines the deformation mode [10]. Although embryonic SB forms when STZs are densely populated within a narrow region, SB can only propagate when its propagation stress is reached [13,15,62]. Within the regime of $h > 10$ nm, it is clearly observed that the amorphous layer is neither thinned remarkably nor shear fractured, even though the layer is compressed to a high strain of 20%. This result indicates that the maximum strength of the C/A pillars is less than that for either SB nucleation or propagation and that the softer Cu layers bear the main plastic deformation at $h > 10$ nm.

However, in micropillars with h equal to or less than 10 nm, barreling of the C/A micropillars is evident, which is accompanied by localized shear deformation that is initiated at geometric stress concentrators, such as pillar corners. Meanwhile, the smooth surface of the compressed C/A pillars reveals that the Cu layers were not squeezed

out as in the large- h pillars. It is suggested that the crystalline layer and the amorphous layer co-deform as the deformation proceeds. The co-deformation between the crystalline and amorphous layers can be attributed to the rapid work-hardening capability of the Cu layer, which is caused by the interaction of glide-interface dislocations [26,40,60]. Unlike the GBs and CCIs that exhibit extreme strain incompatibility, the strain compatibility in the C/A pillars can be easily achieved because the STZs in the amorphous layers are omnidirectional and the CAIs have random structural variation [22]. These mechanisms are most likely the underlying mechanisms for the uniform deformation of the C/A pillars at low strains. Nevertheless, although the localized shear failure can be explained in terms of the dislocation cutting across the CCIs in C/C nanolayered Al/Pd [49] and Cu/Zr [26] micropillars at relatively high strains, this explanation is not applicable to the present nanolayered C/A pillars because the amorphous layers can act as natural sinks for dislocations and absorb the dislocation content in the nanocrystalline Cu [22], which is fundamentally different from the crystalline layers. In this case, the fracture of the amorphous layer most likely promotes the shear banding in the C/A pillars because the external stress is considerably greater than the fracture or ideal strength of the amorphous layer.

4.3.2. Transition in the deformation modes

Next, we provide a quantitative explanation for the experimental results that revealed that homogenous deformation occurs in the C/A pillars when $h > 10$ nm, whereas shear fracture occurs when $h \leq 10$ nm. The strength discrepancy between the two constituent layers, i.e., the nanocrystalline Cu layer and the amorphous layer, is responsible for this transition in deformation modes. The details of the analyses are as follows.

While the initiation of shear banding is controlled by the shear stress (i.e., the embryonic SB forms at the yield strength), the propagation of the SB is governed by the stored elastic energy. To facilitate a quantitative representation of the experimental data, the present authors follow previous energy balance models, where the shear band is treated like a crack driven by the release of all of the stored elastic energy in the sample body [13,15]. Assuming relations that are analogous to the Griffith's crack equation, the critical stresses necessary to drive a SB was derived to be:

$$\sigma_{\text{pro}} = \sqrt{\frac{2\sqrt{2}\Gamma E}{h}} \quad (6)$$

where $\Gamma \sim 0.56 \text{ J m}^{-2}$ [13] is the SB energy density per unit area, $E \sim 90 \text{ GPa}$ is the measured Young's modulus, and h is the thickness of the amorphous layer. Obviously, the stress required to drive a SB propagation (σ_{pro}) increases with decreasing characteristic length (h); see the solid red line in Fig. 5a. Assuming that σ_{pro} has a value equal to the lowest MG yield strength of $\sim 1500 \text{ MPa}$, the intersec-

tion between the $\sigma_{\text{pro}}-h_a$ curve and the lower bound of the MG yield strength range yields a critical size $h_{\text{cri}} \sim 60 \text{ nm}$. This size is the critical characteristic dimension where the deformation mode of the amorphous layer (not the whole pillar) transitions from instantaneous localized shear to homogeneous deformation, with the value consistent with other results [11,13,15–17]. When the characteristic dimension is larger than h_{cri} , the amorphous layer instantaneously fails by shear-band formation, which makes elastic loading followed by catastrophic failure the dominant deformation mode. When the characteristic dimension is small ($< h_{\text{cri}}$), any formed embryonic SB remains stable at the stress required for homogeneous deformation; therefore, homogeneous deformation of the amorphous pillars (not the whole pillar) prevails.

However, when the amorphous layer thickness (h_a) is sufficiently thin, no STZ will grow into a mature SB, as proposed by an aged-rejuvenation-glue-liquid SB model [22,63,64]. This model predicts that the size of the stressed metallic glass region must exceed an incubation length scale h_{inc} to develop STZs into mature SBs:

$$h_{\text{inc}} = \frac{\xi c_v^2 (T_g - T_{\text{env}})^2}{\tau_{\text{glue}}^2 c_s} \quad (7)$$

where ξ is the metallic glass's thermal diffusivity, c_v is its volumetric specific heat, $T_{\text{env}} \approx 300 \text{ K}$ is the ambient temperature, $T_{\text{glue}} \approx 0.01E$ as evaluated from both experimental data and molecular dynamics (MD) simulations [63,64] and $c_s = (\mu/\rho)^{0.5}$ is the shear wave speed. For the present amorphous Cu60Zr40, Eq. (7) gives $h_{\text{inc}} \approx 10 \text{ nm}$. Similar results have been claimed by Cheng et al. [18], where at least 5 nm in size is required for developing an unconstrained SB. Therefore, one can envision that, if the characteristic microstructure size is smaller than the critical size $h_{\text{inc}} \sim 10 \text{ nm}$, it is difficult to develop SBs. Extra stress is progressively required for further deformation of the C/A pillar until to final failure. This reason is why the C/A pillar can achieve a ultrahigh yield stress close to the ideal strength of Cu [45]. Experimental examinations of SBs in bulk metallic glasses also indicate that they have a characteristic thickness of $\sim 10\text{--}100 \text{ nm}$ [1–3,8–10,65,66]. These results, to a certain extent, support the fact that when the thickness of amorphous layer (h_a) is smaller than the intrinsic length scale $h_{\text{inc}} \sim 10 \text{ nm}$, a different mechanical response, i.e., the ceiling strength, may be expected. Because the maximum strength exceeds the ideal strength of the Cu60Zr40 glassy material, the amorphous phase will break. Therefore, we can naturally understand why the shear banding becomes so favorable in C/A pillars below this critical size h_{inc} , even though no SBs will form in the amorphous layers. It is also interesting to observe that h_{inc} appears to exhibit a fair agreement with the deformation mode transition size $\sim 10 \text{ nm}$. The coincidence between above two critical sizes implies a potential natural correlation between STZ-mediated activities (STZ spread-out action and STZ percolation/collection) and the deformation modes.

At present, the size-dependent deformation modes and the transition between them can be well comprehended by referring to Fig. 5a. In this figure, there are two h -dependent strength curves (i.e., the σ_{cls} for dislocation motion and the σ_{pro} for SB propagation) and two h -independent strength/strength ranges (i.e., ideal strength of the Cu60Zr40 glassy material and the yield strength range of the amorphous layer). As previously mentioned, the intersection between the CLS curve and the ideal strength of the Cu60Zr40 glassy material results in a critical size of h_{inc} . This critical size divides the strength-layer thickness map into two regimes, RI and RII. For the C/A pillars where h falls into the RI regime, the SBs cannot form and shear failure will eventually be triggered once the applied stress reaching/exceeding the ideal strength of amorphous Cu60Zr40. Nevertheless, in the RII regime, all of the C/A pillars will display homogeneous-like deformation because their maximum strength is less than the strength ceiling of Cu60Zr40. The glassy phase can deform through SB activities but will not fracture, permitting spatiotemporal deformation of nanocrystalline Cu. In addition, the RII regime is divided into two sub-regimes (i.e., RII-1 and RII-2) by a second critical size, i.e., $h_{\text{cri}} \sim 60$ nm or the intersection between the CLS curve and the lowest amorphous yield strength. In the RII-1 regime of $h_{\text{inc}} < h < h_{\text{cri}}$, the SBs, although can be formed, will be strongly constrained by the deformation of Cu layers. Because the crystalline layer strength and the SB propagation stress are comparable within this regime, the propagation of SBs will be effectively suppressed. This behavior can lead to macroscopic homogeneous-like deformation in the nanolayered C/A pillars. In the RII-2 regime of $h > h_{\text{cri}}$, the maximum strength of C/A pillars will be less than the yield strength of the amorphous phase. No yielding in the amorphous phase hints that there is no possibility to form SBs. Therefore, the crystalline layer is uniformly thinned via symmetric slip activities on multiple slip systems. At this stage, one can state that the deformations in the RII-1 and RII-2 regimes, both are homogeneous-like, have different mechanisms.

5. Conclusions

Systematic investigations have been performed to study the intrinsic size (h) and extrinsic size (ϕ) effects on the compressive deformation of nanolayered crystalline/amorphous Cu/Cu–Zr micropillars within wide ranges of h and ϕ . The results clearly provide deep insights into the size effect on the deformation behavior and the ductile crystalline layer constraining effect on the brittle amorphous layer on the formation/propagation of shear bands. The primary findings can be summarized as follows:

- (1) The mechanical response of the C/A micropillars shifted from initial intrinsic size-controlled strain-hardening to shear-softening at small h or to work-softening at large h . The size-driven strength of the crystalline Cu/amorphous Cu–Zr micropillars

appears to increase in a “smaller is stronger” fashion, which can be broadly described using the confined layer slip model. When h is reduced to less than ~ 10 nm, the deformation mode of the C/A micropillars transitioned from homogeneous extrusion/barreling to localized shear banding, which is also extrinsic size-dependent. The larger pillar is ready to highly inhomogeneous shear, whereas smaller pillar is preferable to relatively homogeneous shear.

- (2) The interplay between the intrinsic and extrinsic size effects induces an ultrahigh strength of ~ 4800 MPa in the nanolayered C/A micropillar with $h = 5$ nm and $\phi = 350$ nm. This strength is considerably larger than the ideal strength of the Cu60Zr40 glassy material and also close to the ideal strength of Cu.
- (3) Due to the existence of nanocrystalline layers, the shear banding instability no longer afflicts the nanoscaled amorphous layers, which act as high capacity sinks for dislocations that contribute to the work-softening. At the same time, the CAIs exhibit unique strain compatibility, which enables the C/A micropillars to homogeneously deform to ultrahigh strain ($>30\%$).

Acknowledgements

This work was supported by the National Natural Science Foundation of China (Grant Nos. 50971097, 51201123), the 973 Program of China (Grant No. 2010CB631003) and the 111 Project of China (B06025). GL thanks the support from Fundamental Research Funds for the Central Universities and Tengfei Scholar project. JYZ thanks China Postdoctoral Science Foundation funded project for part of financial support. The authors wish to thank Prof. X.H. Zhang at Texas A&M University for providing the Cu/Cu–Zr samples. Access to the nanoindentation and FIB equipments in CAMP-Nano is also acknowledged.

References

- [1] Trexler MM, Thadhani NN. Prog Mater Sci 2010;55:759–839.
- [2] Cheng YQ, Ma E. Prog Mater Sci 2011;56:379–473.
- [3] Greer JR, De Hosson JTM. Prog Mater Sci 2011;56:654–724.
- [4] Wang WH. Prog Mater Sci 2012;57:487–656.
- [5] Takeuchi S, Edagawa E. Prog Mater Sci 2011;56:785–816.
- [6] Kocks UF, Mecking H. Prog Mater Sci 2003;48:171–273.
- [7] Nes E. Prog Mater Sci 1997;41:129–93.
- [8] Greer AL, Ma E. MRS Bull 2007;32:611.
- [9] Chen M. Annu Rev Mater Res 2008;38:445–69.
- [10] Schuh CA, Hufnagel TC, Ramamurty U. Acta Mater 2007;55:4067–109.
- [11] Guo H, Yan PF, Wang YB, Tan J, Zhang ZF, Sui ML, et al. Nat Mater 2007;6:735–9.
- [12] Tian L, Cheng YQ, Shan ZW, Li J, Wang CC, Han XD, et al. Nat Commun 2012;3:609.
- [13] Chen CQ, Pei YT, De Hosson JTM. Acta Mater 2010;58:189–200.
- [14] Kuzmin OV, Pei YT, Chen CQ, De Hosson JTM. Acta Mater 2012;60:889–98.
- [15] Jang D, Greer JR. Nat Mater 2010;9:215–9.

- [16] Kim JY, Gu X, Wraith M, Uhl JT, Dahmen KA, Greer JR. *Adv Funct Mater* 2012;22:1972–80.
- [17] Kim JY, Jang DC, Greer JR. *Adv Funct Mater* 2011;21:4550–4.
- [18] Cheng YQ, Ma E. *Acta Mater* 2011;59:1800–7.
- [19] Pauly S, Gorantla S, Wang G, Kühn U, Eckert J. *Nat Mater* 2010;9:473–7.
- [20] Jang JSC, Ciou JY, Hung TH, Huang JC, Du XH. *Appl Phys Lett* 2008;92:011930.
- [21] Hofmann DC, Suh JY, Wiest A, Duan G, Lind ML, Demetriou MD, et al. *Nature* 2008;451:1085–9.
- [22] Wang YM, Li J, Hamza AV, Barbee JTW. *Proc Natl Acad Sci USA* 2007;104:11155–60.
- [23] Liu MC, Lee CJ, Lai YH, Huang JC. *Thin Solid Films* 2010;518:7295–9.
- [24] Donohue A, Spaepen F, Hoagland RG, Misra A. *Appl Phys Lett* 2007;91:241905.
- [25] Zhang JY, Zhang X, Wang RH, Lei SY, Zhang P, Niu JJ, et al. *Acta Mater* 2011;59:7368–79.
- [26] Zhang JY, Lei SY, Liu Y, Niu JJ, Chen Y, Liu G, et al. *Acta Mater* 2012;60:1610–22.
- [27] Zhang JY, Zhang X, Liu G, Zhang GJ, Sun J. *Scripta Mater* 2010;63:101–4.
- [28] Zhang JY, Liu G, Zhang X, Zhang GJ, Sun J, Ma E. *Scripta Mater* 2010;62:333–6.
- [29] Wang J, Misra A. *Curr Opin Solid State Mater Sci* 2011;15:20–8.
- [30] Anderson PM, Li C. *Nanostruct Mater* 1995;5:349–62.
- [31] Misra A, Hirth JP, Kung H. *Philos Mag A* 2002;82:2935–51.
- [32] Phillips MA, Clemens BM, Nix WD. *Acta Mater* 2003;51:3157–70.
- [33] Misra A, Hirth JP, Hoagland RG. *Acta Mater* 2005;53:4817–24.
- [34] Hoagland RG, Kurtz RJ, Henager CH. *Scripta Mater* 2004;50:775–9.
- [35] Misra A, Hoagland RG. *J Mater Sci* 2006;42:1765–71.
- [36] Han SM, Phillips MA, Nix WD. *Acta Mater* 2009;57:4473–90.
- [37] Greer JR, Oliver WC, Nix WD. *Acta Mater* 2005;53:1821–30.
- [38] Bharathula A, Lee SW, Wright WJ, Flores KM. *Acta Mater* 2010;58:5789–96.
- [39] Lee S-W, Han SM, Nix WD. *Acta Mater* 2009;57:4404–15.
- [40] Misra A, Zhang X, Hammon D, Hoagland RG. *Acta Mater* 2005;53:221–6.
- [41] Lei SY, Zhang JY, Niu JJ, Liu G, Zhang X, Sun J. *Scripta Mater* 2012;66:706–9.
- [42] Bhattacharyya D, Mara NA, Dickerson P, Hoagland RG, Misra A. *Acta Mater* 2011;59:3804–16.
- [43] Bei H, Lu ZP, George EP. *Phys Rev Lett* 2004;93:125504.
- [44] Kiener D, Minor AM. *Acta Mater* 2011;59:1328–37.
- [45] Richter G, Hillerich K, Gianola DS, Monig R, Kraft O, Volkert CA. *Nano Lett* 2009;9:3048–52.
- [46] Zhang JY, Zhang X, Liu G, Wang RH, Zhang GJ, Sun J. *Mater Sci Eng A* 2011;528:7774–80.
- [47] Gruber PA, Böhm J, Onuseit F, Wanner A, Spolenak R, Arzt E. *Acta Mater* 2008;56:2318–35.
- [48] Lu L, Chen X, Huang X, Lu K. *Science* 2009;323:607–10.
- [49] Dayal P, Quadir MZ, Kong C, Savvides N, Hoffman M. *Thin Solid Films* 2011;519:3213–20.
- [50] Samuel KG. *J Phys D: Appl Phys* 2006;39:203–12.
- [51] Zhu T, Li J. *Prog Mater Sci* 2010;55:710–57.
- [52] Kumar KS, Van Swygenhoven H, Suresh S. *Acta Mater* 2003;51:5743–74.
- [53] Dao M, Lu L, Asaro RJ, De Hosson JTM, Ma E. *Acta Mater* 2007;55:4041–65.
- [54] Nagarjuna S, Gopalakrishna B, Srinivas M. *Mater Sci Eng A* 2006;429:169–72.
- [55] Chaudhri MM. *Acta Mater* 1998;46:3047–56.
- [56] Zhang JY, Lei S, Niu J, Liu Y, Liu G, Zhang X, et al. *Acta Mater* 2012;60:4054–64.
- [57] Huang X, Hansen N, Tsuji N. *Science* 2006;312:249.
- [58] Ungár T, Li L, Tichy G, Pantleon W, Choo H, Liaw PK. *Scripta Mater* 2011;64:876–9.
- [59] Cammarata RC. *Prog Surf Sci* 1994;46:1–38.
- [60] Donohue A, Spaepen F, Hoagland RG, Misra A. *Appl Phys Lett* 2007;91:241905.
- [61] Arman B, Brandl C, Luo SN, Germann TC, Misra A, Cagin T. *J Appl Phys* 2011;110:043539.
- [62] Cao AJ, Cheng YQ, Ma E. *Acta Mater* 2009;57:5146–55.
- [63] Shimizu F, Ogata S, Li J. *Acta Mater* 2006;54:4293–398.
- [64] Shimizu F, Ogata S, Li J. *Mater Trans* 2007;48:2923–7.
- [65] Zhang Y, Greer AL. *Appl Phys Lett* 2006;89:071907.
- [66] Pan D, Inoue A, Sakurai T, Chen MW. *Proc Natl Acad Sci* 2008;105:14769–72.